High-Performance Tellurium-Free Thermoelectrics: All-Scale Hierarchical Structuring of p-Type PbSe−MSe Systems (M = Ca, Sr, Ba)

Yeseul Lee,[†,⊥] Shih-Han Lo,[‡,⊥] John Androulakis,[†] Chun-I Wu,[§] Li-Dong Zhao,[†] Duck-Young Chung,[‖] Timothy P. Hogan,[§] Vinayak P. Dravid,[‡] and Mercouri G. Kanatzidis*[,†,‖]

[†]Department of Chemistry, Northwestern University, Evanston, Illinois 60208, United States
[‡]Department of Materials Science and Engineering, Northwestern University, Evanston, Illinois 60208, United States
[§]Department of Electrical and Computer Engineering, Michigan State University, East Lansing, Michigan 48824, United States
[‖]Materials Science Division, Argonne National Laboratory, Argonne, Illinois 60439, United States

S *Supporting Information*

ABSTRACT: We present a systematic study of the characterization and thermoelectric properties of nanostructured Na-doped PbSe embedded with 1−4% MSe (M = Ca, Sr, Ba) phases as endotaxial inclusions. The samples were powder-processed by the spark plasma sintering technique, which introduces mesoscale-structured grains. The hierarchical architectures on the atomic scale (Na and M solid solution), nanoscale (MSe nanoprecipitates), and mesoscale (grains) were confirmed by transmission electron microscopy. These structures produce a great reduction in the lattice thermal conductivity relative to pristine PbSe without appreciably affecting the power factor. The lattice thermal conductivity can be reduced by up to ∼29% when the second phase is added. The highest ZT value achieved was ∼1.3 at 923 K for both 2% SrSe-and 3% BaSe-containing samples, while the sample containing 4% CaSe showed a ZT value of ∼1.2 at 923 K. The optimal samples have hole carrier concentration of $1−2 \times 10^{20}$ cm^{-3}. We attribute the high ZT values to the combination of broad-based phonon scattering on multiple length scales and favorable charge transport through coherent interfaces between the PbSe matrix and MSe.
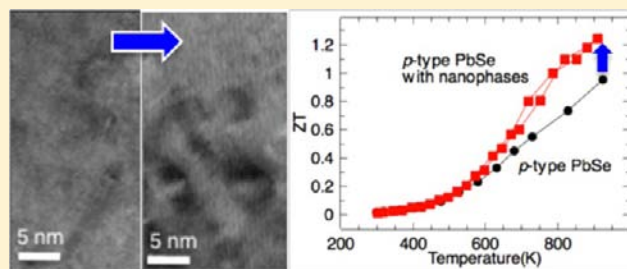
INTRODUCTION

Thermoelectric materials convert temperature differences to electric energy and may have an impact on power management through use of waste heat sources.[1−3] The dimensionless figure of merit for thermoelectric materials is defined as $ZT = (S^2\sigma/\kappa) T$, where T is the absolute temperature, S is the Seebeck coefficient, σ is the electrical conductivity, and κ is the thermal conductivity. The thermoelectric efficiency is defined by combining the figure of merit and the Carnot efficiency. Thus, obtaining a high efficiency requires both high ZT values and a large temperature gradient across the materials. To increase ZT, the materials need to have either a large power factor ($S^2\sigma$), a low thermal conductivity, or both. One way to maximize the power factor of existing semiconducting materials is to modify appropriately their electronic structure close to the Fermi level.[4,5] Reducing the thermal conductivity by embedding nanostructures is an effective way to enhance ZT.[2,6−14] However, the power factor is also reduced relative to the single-phase parent materials because the nanoinclusions increase carrier scattering. Therefore, the challenge in developing materials with superior performance is to tailor the interconnected thermoelectric physical parameters for a crystalline system.

Lead chalcogenides have many compelling attributes as promising thermoelectric materials because they have heavy elements for low thermal conductivities, high carrier mobilities, and highly symmetric structures for high band degeneracy, leading to large power factors. They also exhibit high melting points, providing high operation temperatures and exceptional environmental stability. Research to date on lead chalcogenides has focused mostly on PbTe-based materials. Because Te is rare in the Earth's crust[15] it would be beneficial to develop alternative materials based on chemical elements that are cheaper and more abundant than Te. One attractive alternative is PbSe because Se is less expensive, has longer-term price stability, and is 50 times more abundant than Te.[15] Moreover, PbSe melts at a higher temperature than PbTe (1084 vs 925 °C), which means that a higher efficiency can be anticipated on the basis of higher operating temperatures. High ZT values have recently been reported for several n-type PbSe materials

(ZT = ~0.9 for $Pb_{1-x}[In/Ga]_xSe$ at 900 K, ~1.3 for PbSe:Al at 850 K, and ~1.3 for PbSe−PbS:PbCl$_2$ at 900 K)[11,16,17] and p-type PbSe materials (ZT = ~1.2 for $Pb_{1-x}Na_xSe$ at 850 K and ~1 for $Pb_{1-x}Ag_xSe$ at 770 K),[18,19] indicating that PbSe is a good candidate for viable high-temperature thermoelectric material systems. Theoretical calculations[20] have suggested that heavily doped p-type PbSe could potentially show a ZT value of ~2 at 1000 K, providing further motivation to continue investigations of this system.

In recent studies, we showed that endotaxially embedded alkaline-earth telluride nanocrystals in p-type bulk PbTe greatly enhance phonon scattering without affecting the hole mobility.[21−24] This insensitivity of carrier scattering to the presence of second-phase nanocrystals was attributed to alignment of the valence bands of SrTe and PbTe. The reported ZT values for these systems reached ~2.2 (PbTe-SrTe:Na),[21,24] ~1.5 (PbTe-CaTe:Na), ~1.3 (PbTe-BaTe:Na),[22] and ~1.6 (PbTe-MgTe:Na)[23] for p-type PbTe at ~800 K. We also observed a ZT value of ~1.2 at 923 K for the Na-doped PbS−SrS system.[14] The aforementioned results motivated us to expand our investigations to completely Te-free systems and bring to bear many of the new concepts and ideas developed for PbTe itself that have been so successful in producing record-breaking performance.

In this work, we investigated the high-temperature thermoelectric properties of several compositions of p-type PbSe embedded with nanocrystals of alkaline-earth selenides MSe (M = Ca, Sr, Ba) and doped with Na. Na was chosen as the p-type dopant to tune the carrier concentration by substituting Na^+ for Pb^{2+} to optimize the charge-transport properties of the PbSe matrix. Our data show that the phases of CaSe, SrSe, and BaSe are effective in reducing the lattice thermal conductivity of Na-doped PbSe. We applied the pulsed electric current sintering technique, also known as spark plasma sintering (SPS), to obtain highly dense and robust thermoelectric specimens from mesoscaled powders. This approach allowed us to produce hierarchical nano- and mesoscale-structured phases. As a result, we report a ZT of ~1.3 at 923 K for 2% SrSe- and 3% BaSe-containing samples doped with 1% Na.

■ EXPERIMENTAL SECTION

Reagents. Elemental Pb (99.99%, American Elements), Se (99.999%, 5N Plus Inc.), Na (99.95%, Aldrich), Ca (99.5%, Alfa Aesar), Sr (99.9%, Cerac), and Ba (99.9%, Sigma-Aldrich) were used for the synthesis.

Synthesis. Ingots (~20 g) with nominal compositions $Pb_{0.99/0.98−x}Na_{0.01/0.02}M_xSe$ (M = Ca, Sr, Ba; x = 0.01, 0.02, 0.03, 0.04) were prepared by mixing appropriate ratios of reagents in carbon-coated quartz tubes in a N_2-filled glovebox. The tubes were sealed under vacuum (~10^{-4} Torr), heated to 1150 °C over a period of 12 h, soaked at that temperature for 5 h, slowly cooled to 1080 °C over 12 h, and rapidly cooled to room temperature over 3 h. The obtained ingots were cleaned and ground to a powder using a mortar and pestle to reduce the grain size to smaller than 5 mm^3 and then further ground by a mechanical mortar and pestle to reduce the particle sizes to <53 μm^3. These powders were densified at 650 °C for 10 min under an axial compressive pressure of 60 MPa in an argon atmosphere. Relative densities in the range of 98.3–100.6% of the theoretical values were achieved (see the Supporting Information).

Characterization. Powder X-ray diffraction (PXRD) patterns for all samples were collected using Cu Kα radiation on an INEL diffractometer operating at 40 kV and 20 mA and equipped with a position-sensitive detector.

The samples for measurements of charge-transport properties were cut and polished into parallelepipeds with dimensions of ~2 mm × 3 mm × 10 mm. The electrical conductivity and Seebeck coefficient were measured simultaneously under a helium atmosphere (~0.1 atm) from room temperature to ~923 K using an ULVAC-RIKO ZEM-3 system. Samples measured to 923 K were coated with boron nitride to protect the instrument against evaporation of the elements. Multiple cycles and different specimens produced similar properties. The charge-transport specimens were subsequently used in room-temperature Hall effect measurements to determine their carrier densities under the assumption of a unitary Hall factor, which gives a Hall coefficient $R = 1/ne$, where n is the carrier density and e is the electron charge. Hall coefficients were measured with a home-built system in a magnetic field ranging from 0.5 to 1.25 T, utilizing a simple four-contact Hall bar geometry and both negative and positive polarities of the magnetic field to eliminate Joule resistive errors. Values of the mobility (μ) at room temperature were calculated using the relation $\mu = \sigma/ne$.

A NETZSCH LFA 457 MicroFlash instrument was used to determine the thermal diffusivity of samples that were cut and polished into rectangular parallelepipeds with dimensions of ~2 mm × 10 mm × 10 mm and coated with graphite. The thermal conductivity (κ) was calculated using the relation $\kappa = DC_p\rho$, where D is the thermal diffusivity, C_p is the heat capacity, and ρ is the mass density of the specimen. The ρ values used here were calculated using the geometrical dimensions of the specimens and their masses; the corresponding densities were ≥98% of the theoretical densities. The specific heats of the samples were estimated using established literature values[25] (see the Supporting Information).

Scanning electron microscopy (SEM) studies were performed using a Hitachi S-4800 microscope with an accelerating voltage of 5 kV and a secondary electron detector. Transmission electron microscopy (TEM) investigations were carried out on a JEOL 2100F microscope operated at 200 kV. The thin TEM specimens were prepared by conventional methods, including cutting, grinding, dimpling, polishing, and Ar-ion milling on a liquid nitrogen cooling stage.

■ RESULTS AND DISCUSSION

A. Structural Characterization. Since the phase diagrams of PbSe−MSe systems are unknown, ingots were heated to 1150 °C, which was sufficient to melt all of the elements, and the liquid was air-quenched. Figure 1a presents the PXRD patterns of PbSe−CaSe:Na samples (patterns for PbSe−SrSe:Na and PbSe−BaSe:Na are given in Figure S1 in the Supporting Information). All of the patterns were indexed in the NaCl structure ($Fm\overline{3}m$ space group) without any noticeable second phase for MSe contents of up to 4 mol %. Figure 1b depicts the extracted lattice parameters as functions of MSe content. The lattice parameter of PbSe (6.128 Å) decreases with increasing CaSe (5.92 Å) content but increases with rising SrSe (6.22 Å) and BaSe (6.6 Å) contents. This is Vegard's law behavior, and it is consistent with size trends and indicates some solubility of the alkaline-earth ions in the lattice. As we will show below, however, there is also nanostructuring in the PbSe matrix that is detectable with TEM. No MSe or other phases were observed at MSe contents of up to 4 mol % within the detection limits of our X-ray diffraction equipment. Figure 1c shows a typical SPS disk-shaped pellet and cut and polished samples for measurements in this study.

B. Charge Carrier Concentrations and Thermoelectric Properties at 300 K. Na was used as a p-type dopant in this study, and from simple valence electron counting, each Na atom is expected to add one p-type carrier. Figure 2 shows the experimental room-temperature Hall carrier concentrations as functions of Na concentration. The theoretical Hall carrier concentration as calculated using simple valence electron counting is shown as a solid line for comparison. The values of the Hall coefficient are positive, consistent with p-type
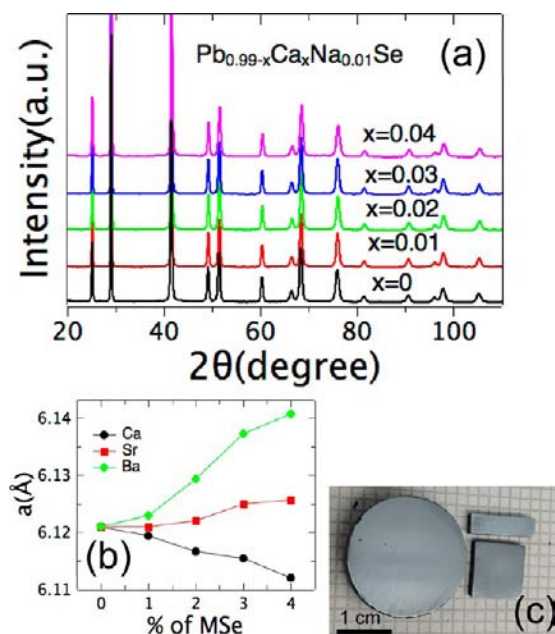
Figure 1. (a) PXRD patterns for samples of PbSe—CaSe:Na. (b) Lattice parameters as functions of MSe content (M = Ca, Sr, Ba). (c) Typical SPS pellet and samples used in this study.
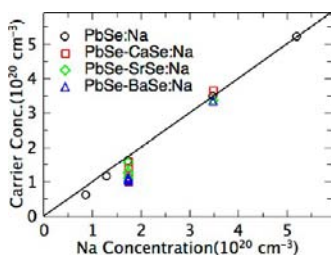

Figure 2. Hall effect charge carrier concentration in PbSe—CaSe, PbSe—SrSe, PbSe—BaSe, and pristine PbSe doped with 0.5—3% Na. The solid line is the predicted carrier concentration.

conduction. Increasing the amount of dopant increased the Hall carrier concentration, as expected. Collectively, the Hall measurements suggested that the maximum solubility of Na is not reached up to 3 mol % Na, since the Hall carrier concentration increased linearly with increasing Na.

Figure 3 shows the room-temperature hole mobilities (μ_H) as functions of Hall charge carrier concentration for PbSe—MSe samples doped with 1 and 2% Na. Some control samples of PbSe with no MSe and doped with x% Na (x = 0.5, 0.75, 1, 2, 3) are also plotted for comparison. The black dashed line shows the behavior of the pristine single-phase PbSe system. The PbSe—CaSe and PbSe—SrSe samples with ≤3% CaSe and SrSe fall on the same curve as the data for pristine PbSe. However, samples of PbSe with 2—4% BaSe and 4% CaSe or SrSe fall well below the mobility values of the pristine systems. Figure 3b is an enlarged image of the rectangle in Figure 3a, and the symbols C1—B4 on the graph correspond to Table 1, where the samples used in the present study are listed according to composition. Thus, for similar carrier concentrations adding heavier alkaline-earth elements and higher MSe contents in PbSe decrease the hole mobility relative to that of pristine PbSe. However, this observation also indicates that the carrier transport is not greatly affected when the MSe content is as high as 3% for CaSe and SrSe and 1% for BaSe. For 2% Na
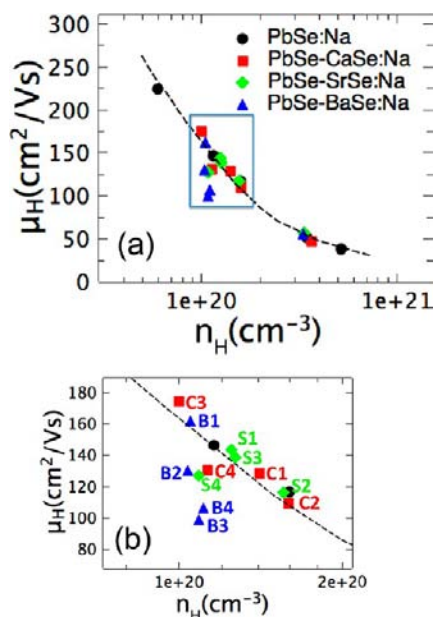

Figure 3. (a) Hole mobilities as functions of carrier concentration at room temperature for samples of PbSe—CaSe, PbSe—SrSe, PbSe—BaSe, and pristine PbSe doped with 0.5—3% Na. The black dashed line is a guide for the eye for the pristine PbSe system. (b) Enlarged image of the rectangle in (a).

doping, all of the PbSe—1%MSe samples showed the same mobility of ∼50 cm² V⁻¹ s⁻¹ at 300 K, consistent with that of pristine PbSe doped with 2% Na.

Figure 4 shows a room temperature Pisarenko plot (Seebeck coefficient vs Hall carrier concentration) for PbSe—MSe and PbSe doped with 0.5, 0.75, 1, 2, and 3% Na. The mobility values vary with the type and fraction of alkaline-earth metal, but the Seebeck coefficient is insensitive to these factors. The dashed black line in Figure 4 is based on a model employing a single parabolic band with a PbSe light-hole effective mass of $m^*/m_0 = 0.36$, where m^*/m_0 is the density-of-states effective mass and acoustic phonon scattering has been assumed as the main carrier scattering mechanism ($r = -0.5$).[13,14] The deviation from the calculated line at higher concentration is attributed to nonparabolicity of the PbSe light-hole band and probably a contribution from the second so-called heavy-hole valence band.[26] The experimentally determined values and the Pisarenko line show excellent agreement regardless of MSe fraction, suggesting that there is no particular enhancement of the Seebeck coefficient by these second-phase nanostructures.

C. Temperature-Dependent Charge-Transport Properties. Figure 5 depicts the temperature-dependent electrical conductivities of PbSe—MSe samples doped with 1% Na and control sample doped with 1% Na but without MSe. For all of the samples, the electrical conductivity decreases with increasing temperature, consistent with previous observations for heavily doped semiconductors with metallic transport behaviors. With increasing MSe fraction, the electrical conductivity shows a decreasing trend, corresponding to a decrease in mobility at lower temperature. However, the electrical conductivity shows almost no reduction at high temperature (≳800 K).

Figure 6 shows the Seebeck coefficients of PbSe—MSe samples doped with 1% Na and a 1% Na-doped control sample as functions of temperature. The Seebeck coefficients are positive over the entire temperature range, indicating p-type

Table 1. Room-Temperature Carrier Concentrations (n_H), Hole Mobilities (μ_H), Seebeck Coefficients (S), Electrical Conductivities (σ), Lattice Thermal Conductivities (κ_{lat}), and Figures of Merit (ZT) at 923 K for 1% Na-Doped PbSe−MSe Samples

| sample	ID	n_H (10^{20} cm^{-3})	μ_H (cm^2 V^{-1} s^{-1})	S (μV/K)	σ (S/cm)	κ_{lat} (W/mK)		ZT
						300 K	923 K	
$Pb_{0.99}Na_{0.01}Se$	M0	1.6	135	29	2981	2.14	0.85	0.95
$Pb_{0.98}Ca_{0.01}Na_{0.01}Se$	C1	1.4	128	20	2880	1.88	0.79	1.13
$Pb_{0.97}Ca_{0.01}Na_{0.02}Se$	C1−2	3.7	47	22	2868	1.83	0.81	0.93
$Pb_{0.97}Ca_{0.02}Na_{0.01}Se$	C2	1.6	110	28	2789	1.71	0.77	0.94
$Pb_{0.96}Ca_{0.03}Na_{0.01}Se$	C3	1.0	175	32	2794	1.54	0.74	0.96
$Pb_{0.95}Ca_{0.04}Na_{0.01}Se$	C4	1.1	129	41	2324	1.35	0.7	1.21
$Pb_{0.98}Sr_{0.01}Na_{0.01}Se$	S1	1.3	143	31	2869	1.71	0.78	1.17
$Pb_{0.97}Sr_{0.01}Na_{0.02}Se$	S1−2	3.4	56	20	3017	1.74	0.77	0.88
$Pb_{0.97}Sr_{0.02}Na_{0.01}Se$	S2	1.6	116	24	2901	1.59	0.73	1.26
$Pb_{0.96}Sr_{0.03}Na_{0.01}Se$	S3	1.3	224	48	2135	1.41	0.68	1.18
$Pb_{0.95}Sr_{0.04}Na_{0.01}Se$	S4	1.1	139	36	2415	1.24	0.67	1.01
$Pb_{0.98}Ba_{0.01}Na_{0.01}Se$	B1	1.1	162	29	2716	1.58	0.75	1.11
$Pb_{0.97}Ba_{0.01}Na_{0.02}Se$	B1−2	3.3	55	24	2952	1.58	0.74	0.89
$Pb_{0.97}Ba_{0.02}Na_{0.01}Se$	B2	1.0	131	31	2172	1.44	0.67	1.03
$Pb_{0.96}Ba_{0.03}Na_{0.01}Se$	B3	1.1	99	37	1725	1.33	0.64	1.27
$Pb_{0.95}Ba_{0.04}Na_{0.01}Se$	B4	1.1	106	30	1888	1.23	0.63	0.99
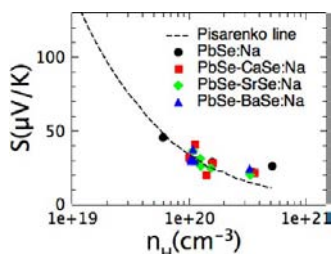
Figure 4. Room-temperature Pisarenko plot for samples of PbSe−CaSe, PbSe−SrSe, PbSe−BaSe, and pristine PbSe doped with 0.5−3% Na. The dashed black line is based on a model employing a single parabolic band[13] with a PbSe effective mass of $m^*/m_0 = 0.36$.

conduction. The thermoelectric power increases monotonically with temperature and reaches ~250 μV/K at 923 K. There is no sign of saturation of the thermoelectric power up to 923 K, indicating the absence of significant bipolar diffusion. The Seebeck coefficients show negligible changes with the nature of the metal selenide added as a second phase and reflect the excellent control of the carrier concentration through the fixed Na doping content (Table 1). The thermoelectric power values at 923 K range from ~240 to ~260 μV/K.

Figure 7 presents power factors derived from the electrical conductivities and Seebeck coefficients as functions of temperature for PbSe−MSe samples doped with 1% Na and a 1% Na-doped PbSe control sample. All of these samples showed similar power factors ranging from ~10 to ~14 μW cm^{-1} K^{-2} at 923 K.

To see the effect of higher carrier concentrations on the power factor, we also investigated 2% Na-doped PbSe samples with 1% MSe (Figure S2 in the Supporting Information). The 2% Na-doped samples have higher electrical conductivities and lower thermoelectric power values consistent with the higher carrier density, and the power factors are similar to those of 1% Na-doped samples.

D. Thermal Conductivity. Values of the total thermal conductivity (κ_{tot}) for all of the samples as functions of temperature are shown in Figure 8. The total thermal conductivity, which consists of contributions from the charge
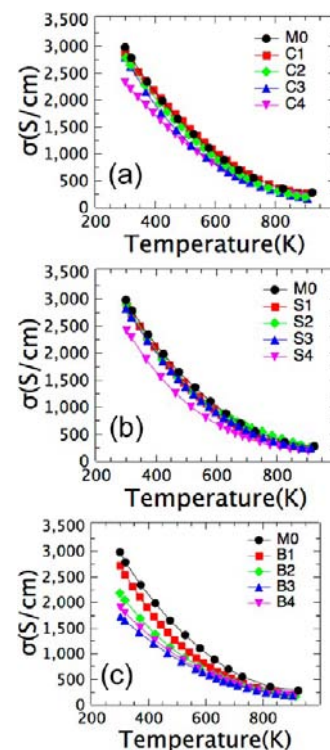

Figure 5. Electrical conductivities as functions of temperature for (a) $Pb_{0.99-x}Ca_xNa_{0.01}Se$, (b) $Pb_{0.99-x}Sr_xNa_{0.01}Se$, and (c) $Pb_{0.99-x}Ba_xNa_{0.01}Se$.

carriers and the lattice phonons, decreases with increasing MSe content. At room temperature, the total thermal conductivity decreases from ~4.27 W/mK for $Pb_{0.99}Na_{0.01}Se$ to ~2.55 W/mK for samples containing 3 and 4% BaSe, and these values decreased to ~1.25 and ~0.88 W/mK, respectively, at 923 K.

The lattice thermal conductivity (κ_{lat}) was obtained by subtracting the charge carrier thermal conductivity (κ_{el}) from κ_{tot}. The carrier thermal conductivity was derived from the Wiedemann−Franz relation $\kappa_{el} = L\sigma T$, where L is the Lorenz number. Values of L (Figure S3) were calculated from values of
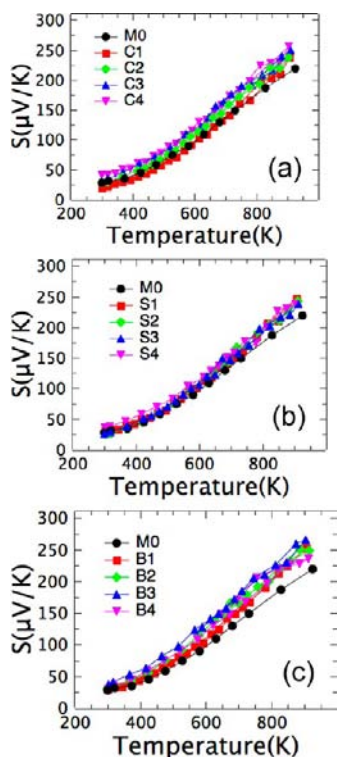
Figure 6. Seebeck coefficients as functions of temperature for (a) $Pb_{0.99-x}Ca_xNa_{0.01}Se$, (b) $Pb_{0.99-x}Sr_xNa_{0.01}Se$, and (c) $Pb_{0.99-x}Ba_xNa_{0.01}Se$.
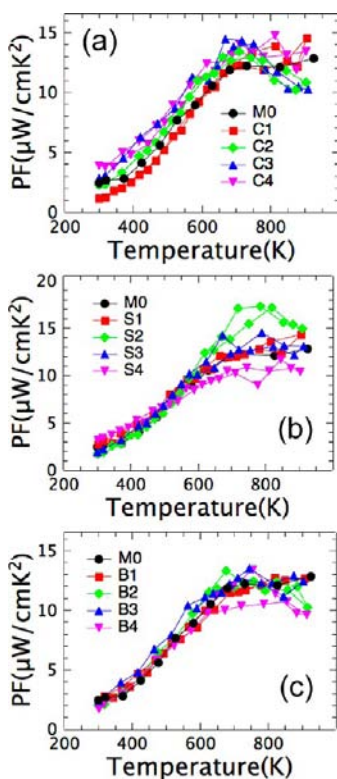

Figure 7. Thermoelectric power factors (PFs) as functions of temperature for (a) $Pb_{0.99-x}Ca_xNa_{0.01}Se$, (b) $Pb_{0.99-x}Sr_xNa_{0.01}Se$, and (c) $Pb_{0.99-x}Ba_xNa_{0.01}Se$.

the chemical potential estimated from fits of the Seebeck coefficients, as explained in detail previously.[12,16] The values of
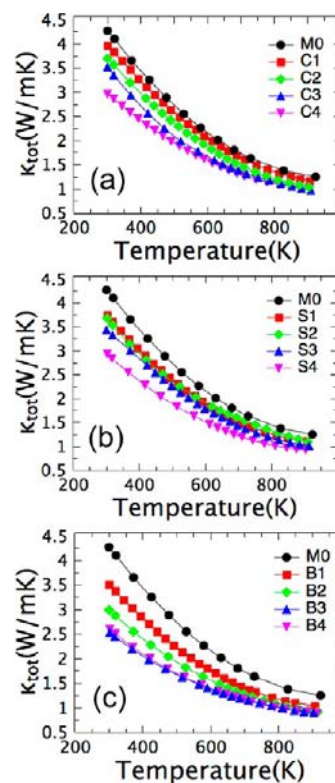

Figure 8. Total thermal conductivities as functions of temperature for (a) $Pb_{0.99-x}Ca_xNa_{0.01}Se$, (b) $Pb_{0.99-x}Sr_xNa_{0.01}Se$, and (c) $Pb_{0.99-x}Ba_xNa_{0.01}Se$.

κ_{lat} for 1% Na-doped PbSe−MSe samples and a control sample with no MSe (Figure 9) decrease with increasing temperature
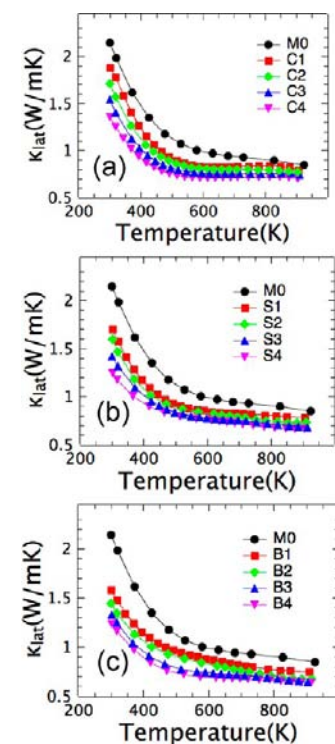

Figure 9. Lattice thermal conductivities as functions of temperature for (a) $Pb_{0.99-x}Ca_xNa_{0.01}Se$, (b) $Pb_{0.99-x}Sr_xNa_{0.01}Se$, and (c) $Pb_{0.99-x}Ba_xNa_{0.01}Se$.

and plateau at high temperature. For all of the samples, κ_{lat} decreases as the alkaline-earth selenide becomes heavier and for a given system decreases with higher MSe content. The room-temperature lattice thermal conductivity decreases from ~2.14 W/mK for pristine PbSe doped with Na to ~1.23 W/mK for the 4% BaSe sample, and these values decreased to 0.85 and 0.63 W/mK, respectively, at 923 K. Thus, a significantly reduced lattice thermal conductivity can be achieved by introducing CaSe, SrSe, and BaSe phases into PbSe.

It is instructive to compare how the lattice thermal conductivities of the three Na-doped lead chalcogenides (PbTe, PbSe, and PbS) are affected by the insertion of alkaline-earth chalcogenides. For example, in the case of Na-doped materials containing SrQ (Q = Te, Se, S) as a second phase, the lattice thermal conductivities of PbTe-, PbSe-, and PbS-based systems are depicted in Figure 10a as functions of
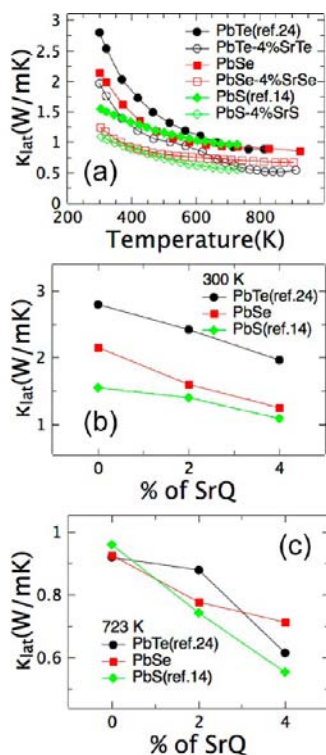

Figure 10. (a) Temperature-dependent lattice thermal conductivities Na-doped PbQ samples containing 0% and 4% SrQ (Q = Te, Se, S). (b, c) Comparison of κ_{lat} values at (b) 300 and (c) 723 K for PbQ samples containing 0, 2, and 4% SrQ. All of the samples were processed using the SPS technique.

temperature and in Figure 10b,c as functions of SrQ fraction at 300 and 723 K, respectively. Regardless of Q, introducing SrQ into the PbQ matrix significantly reduces the thermal conductivity. Introducing 4% SrQ reduced the thermal conductivity at 300 K by ~0.83, 0.90, and 0.45 W/mK (30, 42, and 29% of the values for pristine Na-doped PbQ at 300 K) for the PbTe, PbSe, and PbS systems, respectively. The thermal conductivity at 723 K was reduced by ~0.31, 0.21, and 0.41 W/mK (33, 23, and 42% of the values for pristine Na-doped PbQ at 700 K) by adding 4% SrQ into the PbTe, PbSe, and PbS matrixes, respectively. The total reductions at 723 K after adding 4% SrQ were ~2.18, 1.43, and 0.99 W/mK (78, 67, and 64%) relative to the values for pristine Na-doped PbTe, PbSe, and PbS, respectively, at 300 K.

As shown below, by combining TEM studies and a modified Callaway model,[27] we calculated the lattice thermal conductivity of the p-type nanostructured PbSe system. Comparison of the calculated and experimental data allowed the roles of the nanostructures in reducing the lattice thermal conductivity to be differentiated and understood.[28]

E. Meso/Nanostructures. Typical low- and medium-magnification TEM images of representative PbSe-based samples are shown in Figure 11. The low-magnification TEM
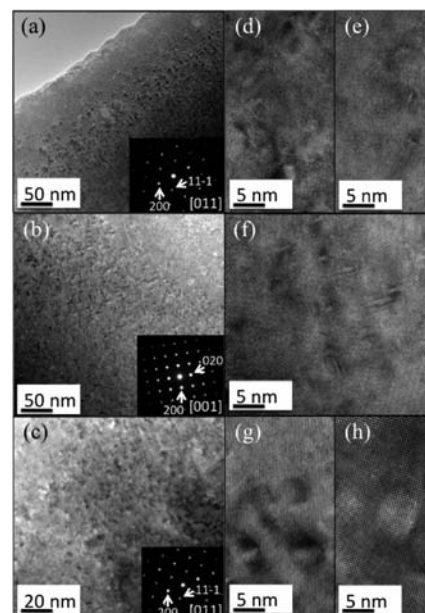

Figure 11. (a−c) Low-magnification TEM images of (a) $Pb_{0.99}Na_{0.01}Se$, (b) $Pb_{0.98}Ba_{0.01}Na_{0.01}Se$, and (c) $Pb_{0.95}Ba_{0.04}Na_{0.01}Se$. The insets show the SAED patterns. (d−h) Medium-magnification TEM images of (d, e) $Pb_{0.99}Na_{0.01}Se$ along the (d) [011] and (e) [001] zone axes, (f) $Pb_{0.98}Ba_{0.01}Na_{0.01}Se$ along the [001] zone axis, and (g, h) $Pb_{0.95}Ba_{0.04}Na_{0.01}Se$ along the (g) [011] and (h) [001] zone axes.

image of 1% Na-doped PbSe (control sample) along the [011] zone axis (Figure 11a) shows the dark contrast of precipitates. When the electron beam was parallel to the [011] zone axis (Figure 11d), most of the precipitates appeared with a quasi-circular shape, but when the beam was projected along [001] (Figure 11e), most of the precipitates appeared as dark lines with lengths of a few nanometers. This can be explained by the fact that the precipitates have a platelet shape and are parallel to the {100} planes, as was observed in the case of alkali-metal-doped PbTe.[30] As with the Na-doped PbTe system, we suggest that the lattice thermal conductivity exhibits more or less the behavior of the pristine compound because the crystallographic structure and mass density of the platelet-like Na-rich precipitates are close to those of the PbSe matrix and do not present adequate impedance to acoustic phonons.

The low-magnification images of 1% Na-doped PbSe samples containing 1% and 4% BaSe (Figure 11b,c) show the dark contrast of precipitates. In the corresponding selected-area electron diffraction (SAED) patterns (insets in Figure 11b,c), which include both the matrix and the precipitates, only the Bragg spots of PbSe can be observed, indicating the good crystallographic alignment (endotaxy) of the nanoprecipitate and matrix lattices. The coexistence of platelet and spherical shapes of the nanoprecipitates for the 1% and 4% BaSe

specimens was confirmed by the medium-magnification images shown in Figure 11f–h. As indicated in Figure 11c, the 1% Na-doped PbSe sample containing 4% BaSe has a high number density of precipitates ($\sim 3.05 \times 10^{17}$ cm^{-3}), and the average size is $\sim$4.5 nm. The existence of Ba was confirmed by energy-dispersive spectroscopy (EDS) (Figure 12). The intensity of
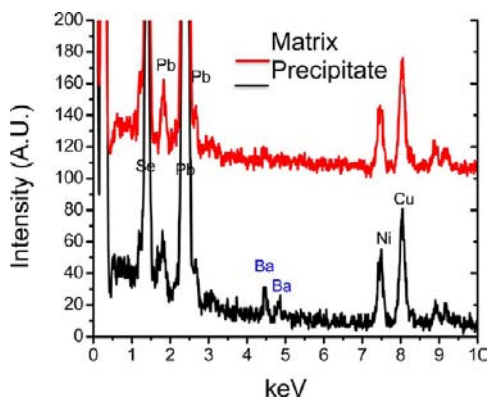

Figure 12. EDS spectra of $Pb_{0.95}Ba_{0.04}Na_{0.01}Se$ samples from the matrix and the precipitate.

the Ba peak was stronger when the beam was sparked at the precipitate than at the matrix. This also indicates that a small amount of Ba dissolved in the PbSe matrix, thus forming the solid solution $Pb_{1-x}Ba_xSe$. According to the TEM observations, the solubility limit of BaSe in PbSe is $\sim$2.7%.

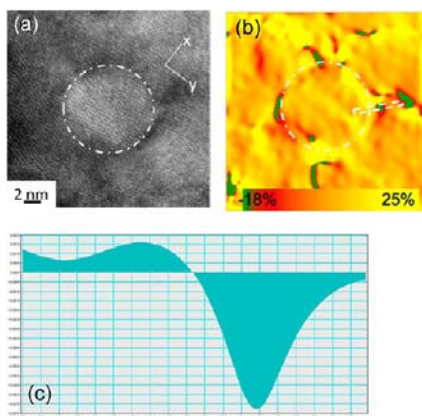A high-resolution TEM (HRTEM) lattice image of 1% Na-doped PbSe containing 4% BaSe is shown in Figure 13a.

Figure 13. (a) HRTEM image of the $Pb_{0.95}Ba_{0.04}Na_{0.01}Se$ sample. (b) The ε_{yy} strain map of the image in (a). (c) The line-scan profile of the region marked in (b).

Information about the strain field was extracted from this image using geometric phase analysis (GPA).[31] The representative tensile in-plane strain field ε_{yy} corresponding to the y direction indicated in Figure 13a is shown in Figure 13b, and 13c depicts the corresponding line-scan profile of the region marked in Figure 13b. The strain map indicates the existence of elastic strain around the precipitate, and the line profile shows a difference of $\sim$8% in the lattice parameters for the two phases.

Mesoscale grain structure achieved by SPS can effectively decrease the value of κ_{lat} beyond what nanostructuring is able to achieve.[24] An SEM image of a Na-doped PbSe sample containing 4% BaSe as synthesized by SPS (Figure 14a)
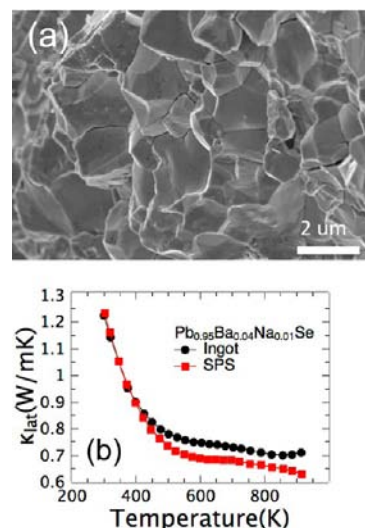

Figure 14. (a) SEM image showing mesoscale grains in a $Pb_{0.95}Ba_{0.04}Na_{0.01}Se$ sample. (b) Comparison of lattice thermal conductivities for SPS and ingot samples of $Pb_{0.95}Ba_{0.04}Na_{0.01}Se$.

shows mesoscale grains with an average size of $\sim$1 μm. It is believed that mesoscale grains in this system (denoted as "SPS" in Figure 14b) scatter phonons with longer mean free paths, further reducing κ_{lat} compared with nanostructuring alone ("Ingot") (Figure 14b and Figure S7 in the Supporting Information).

To provide a further understanding of the mechanism of the meso/nanostructure-reduced lattice thermal conductivity, a theoretical calculation of the lattice thermal conductivity based on a modified Callaway model[27,32] was carried out. According to the Callaway model, the lattice thermal conductivity is expressed as

$$\kappa_{lat} = \frac{k_B}{2\pi^2 c}\left(\frac{k_B T}{\hbar}\right)^3 \int_0^{\theta_D/T} \tau_c \frac{e^x}{(e^x - 1)^2} x^4 \, dx \tag{1}$$

where x is defined as $\hbar\omega/k_B T$, k_B is Boltzmann's constant, $\hbar$ is Planck's constant, c is an average phonon group velocity, θ_D is the Debye temperature, and τ_c is the overall relaxation time. On the basis of TEM studies, scattering from normal (N) and Umklapp (U) processes, boundaries (B), precipitates (P), strains (S), and point defects (PD) contribute to τ_c, according to the equation

$$\tau_c^{-1} = \tau_N^{-1} + \tau_U^{-1} + \tau_B^{-1} + \tau_P^{-1} + \tau_S^{-1} + \tau_{PD}^{-1} \tag{2}$$

To determine the relaxation times for normal and Umklapp processes, we first fitted our calculated data to the experimental ones (blue curves in Figure 15a). Other parameters were obtained from our TEM studies and refs 29 and 33. The results of calculation for 1% Na-doped PbSe containing 4% BaSe (red curve in Figure 15a) shows good agreement with the experimental data. Furthermore, Figure 15b illustrates the relaxation times of the individual processes, providing strong evidence that structures on different scales are important for reducing κ_{lat} in different ranges of phonon frequency. Overall, adding the 4% BaSe second phase produced almost 47% of the reduction at 300 K and 29% at 700 K.

F. Thermoelectric Figure of Merit. The temperature dependence of ZT for the PbSe–MSe samples doped with 1% Na is plotted in Figure 16. For comparison, data for control samples containing no MSe from both this study and a recent
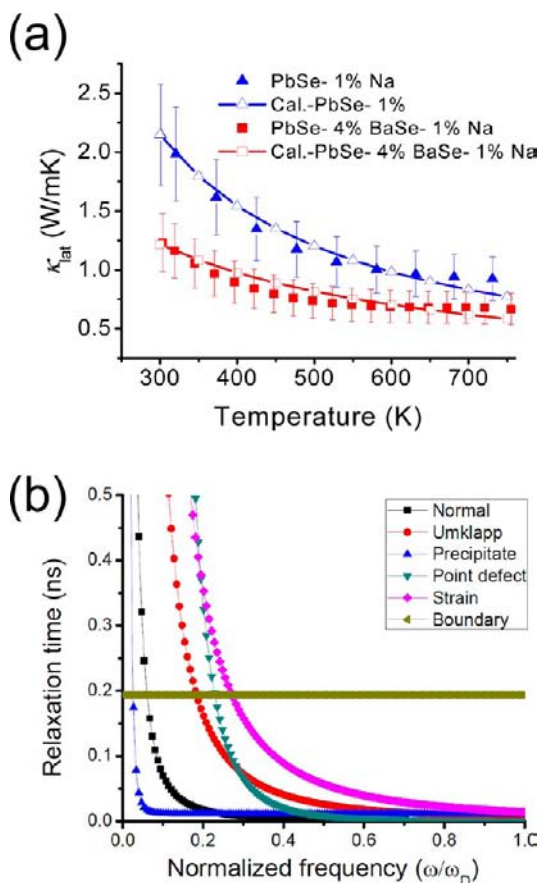
Figure 15. (a) Temperature dependence of the calculated and experimental lattice thermal conductivities of $Pb_{0.99}Na_{0.01}Se$ and $Pb_{0.95}Ba_{0.04}Na_{0.01}Se$. (b) Plot of relaxation times vs normalized phonon frequency for the $Pb_{0.95}Ba_{0.04}Na_{0.01}Se$ sample at 300 K.
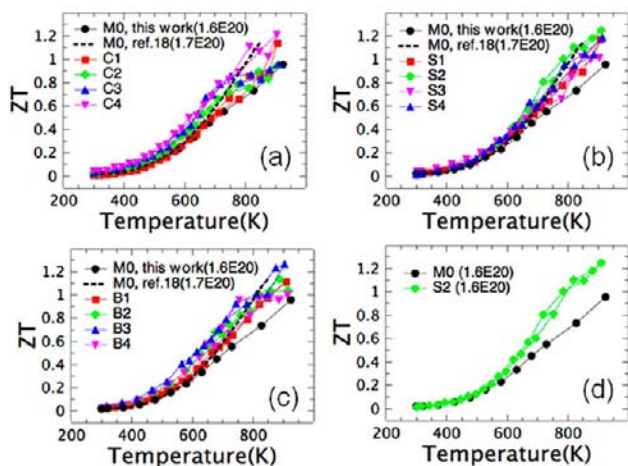

Figure 16. (a−c) Dimensionless figures of merit for (a) $Pb_{0.99-x}Ca_xNa_{0.01}Se$, (b) $Pb_{0.99-x}Sr_xNa_{0.01}Se$, and (c) $Pb_{0.99-x}Ba_xNa_{0.01}Se$. The dashed lines for Na-doped PbSe samples with carrier concentrations of 1.7×10^{20} cm^{-3} reported in ref 18 have been added for comparison. (d) Comparison of ZT values for the PbSe control sample ($Pb_{0.99}Na_{0.01}Se$) and a sample containing 2% SrSe ($Pb_{0.97}Sr_{0.02}Na_{0.01}Se$) at the same carrier concentration (1.6×10^{20} cm^{-3}).

report[18] are also included in the graphs. ZT for a 1% Na-doped PbSe control sample without MSe was less than 1 at 923 K,

while a ZT value of ~1.2 at 850 K was reported[18] at a similar charge carrier concentration (1.7×10^{20} cm^{-3} in ref 18 vs 1.6×10^{20} cm^{-3} here). The thermal conductivity values reported in the previous study are much lower than the values observed here and even lower than the values for our MSe-containing systems. It is not clear whether the different processing methods (SPS vs hot pressing) could have resulted in grain size differences that would account for the thermal conductivity difference. Thus, within the error uncertainty of our measurements, we have not been able to reproduce the ZT value of ~1.2 reported in ref 18 for Na-doped PbSe without MSe added as a second phase. The highest values ZT for the three MSe systems were ~1.2, ~1.3, and ~1.3 at 923 K for samples containing 4% CaSe, 2% SrSe, and 3% BaSe, respectively.

■ CONCLUSIONS

The addition of a few mole percent of the rock-salt phases CaSe, SrSe, and BaSe into PbSe generates endotaxial nanostructuring that causes a reduction of the lattice thermal conductivity without significantly deteriorating the charge-transport properties. The added effects of mesoscale grain boundaries created by SPS processing further decrease the lattice thermal conductivity. In combination with the atomic-scale point defects created by Na doping and M solubility, this all-scale hierarchical structuring allows a significant boost in performance. As a result, a high ZT value of 1.3 was achieved for this system at 923 K. The previously reported ZT value of 1.2 in single-phase p-type PbSe[18] could not be achieved in this work. Nevertheless, it is apparent that PbSe-based materials are emerging as promising, less expensive alternatives to PbTe that have the potential to produce energy conversion devices with good thermoelectric performance at higher operating temperatures than are possible with PbTe-based materials. Theoretical calculations have suggested that heavily doped p-type PbSe may be capable of ZT values as high as ~2.[20] Thus, there may be further room for optimization, as it appears feasible to obtain high-ZT bulk-PbSe-based materials. This could be done by increasing the power factor through modification of the electronic density of states by adding a tertiary or quaternary solute. Another approach could involve a further reduction of the lattice thermal conductivity through optimization of multiscale hierarchical architectures by, for example, controlling the grain and nanoprecipitate sizes.

■ ASSOCIATED CONTENT

Ⓢ Supporting Information

Densities of samples included in the study (Table S1); PXRD patterns of $Pb_{0.99-x}Sr_xNa_{0.01}Se$ and $Pb_{0.99-x}Ba_xNa_{0.01}Se$ (Figure S1); thermoelectric properties as a function of temperature of 1 and 2% Na-doped PbSe−1%MSe, including σ, S, power factor, κ_{tot}, κ_{lat}, and ZT (Figure S2); temperature dependence of L for $Pb_{0.99-x}Ca_xNa_{0.01}Se$, $Pb_{0.99-x}Sr_xNa_{0.01}Se$, and $Pb_{0.99-x}Ba_xNa_{0.01}Se$ (Figure S3); temperature dependence of C_p for $Pb_{0.99-x}Ca_xNa_{0.01}Se$, $Pb_{0.99-x}Sr_xNa_{0.01}Se$, and $Pb_{0.99-x}Ba_xNa_{0.01}Se$ (Figure S4); temperature dependence of D for $Pb_{0.99-x}Ca_xNa_{0.01}Se$, $Pb_{0.99-x}Sr_xNa_{0.01}Se$, and $Pb_{0.99-x}Ba_xNa_{0.01}Se$ (Figure S5); temperature dependence of κ_{el} for $Pb_{0.99-x}Ca_xNa_{0.01}Se$, $Pb_{0.99-x}Sr_xNa_{0.01}Se$, and $Pb_{0.99-x}Ba_xNa_{0.01}Se$ (Figure S6); comparison of κ_{lat} for SPS and ingot samples with same composition (Figure S7); low-magnification TEM image of $Pb_{0.95}Ba_{0.04}Na_{0.01}Se$ along the [001] zone axis (Figure S8); and size distribution histogram of BaSe nanoprecipitates for a $Pb_{0.95}Ba_{0.04}Na_{0.01}Se$ sample (Figure

S9). This material is available free of charge via the Internet at http://pubs.acs.org.

AUTHOR INFORMATION

Corresponding Author
m-kanatzidis@northwestern.edu

Author Contributions
[1]Y.L. and S.-H.L. contributed equally.

Notes
The authors declare no competing financial interest.

REFERENCES

(1) Bell, L. E. *Science* **2008**, *321*, 1457.

(2) Sootsman, J. R.; Chung, D. Y.; Kanatzidis, M. G. *Angew. Chem., Int. Ed.* **2009**, *48*, 8616.

(3) Kanatzidis, M. G. *Chem. Mater.* **2010**, *22*, 648.

(4) Heremans, J. P.; Wiendlocha, B.; Chamoire, A. M. *Energy Environ. Sci.* **2012**, *5*, 5510.

(5) Heremans, J. P.; Jovovic, V.; Toberer, E. S.; Saramat, A.; Kurosaki, K.; Charoenphakdee, A.; Yamanaka, S.; Snyder, G. J. *Science* **2008**, *321*, 554.

(6) Vineis, C. J.; Shakouri, A.; Majumdar, A.; Kanatzidis, M. G. *Adv. Mater.* **2010**, *22*, 3970.

(7) Hsu, K. F.; Loo, S.; Guo, F.; Chen, W.; Dyck, J. S.; Uher, C.; Hogan, T. P.; Polychroniadis, E. K.; Kanatzidis, M. G. *Science* **2004**, *303*, 818.

(8) (a) Poudel, B.; Hao, Q.; Ma, Y.; Lan, Y.; Minnich, A.; Yu, B.; Yan, X.; Wang, D.; Muto, A.; Vashaee, D.; Chen, X.; Liu, J.; Dresselhaus, M. S.; Chen, G.; Ren, Z. *Science* **2008**, *320*, 634. (b) Narducci, D.; Selezneva, E.; Cerofolini, G.; Frabboni, S.; Ottaviani, G. *Journal of Solid State Chemistry* **2012**, *193*, 19−25. (c) Perlt, S.; Hoche, T.; Dadda, J.; Muller, E.; Pereira, P. B.; Hermann, R.; Sarahan, M.; Pippel, E.; Brydson, R. *Journal of Solid State Chemistry* **2012**, *193*, 58−63.

(9) Poudeu, P. F. P.; D'Angelo, J.; Downey, A. D.; Short, J. L.; Hogan, T. P.; Kanatzidis, M. G. *Angew. Chem., Int. Ed.* **2006**, *45*, 3835.

(10) Androulakis, J.; Hsu, K. F.; Pcionek, R.; Kong, H.; Uher, C.; D'Angelo, J. J.; Downey, A.; Hogan, T.; Kanatzidis, M. G. *Adv. Mater.* **2006**, *18*, 1170.

(11) Androulakis, J.; Todorov, I.; He, J.; Chung, D. Y.; Dravid, V. P.; Kanatzidis, M. G. *J. Am. Chem. Soc.* **2011**, *133*, 10920.

(12) Johnsen, S.; He, J.; Androulakis, J.; Dravid, V. P.; Todorov, I.; Chung, D. Y.; Kanatzidis, M. G. *J. Am. Chem. Soc.* **2011**, *133*, 3460.

(13) (a) Zhao, L.-D.; Lo, S.-H.; He, J.; Li, H.; Biswas, K.; Androulakis, J.; Wu, C.-I.; Hogan, T. P.; Chung, D.-Y.; Dravid, V. P.; Kanatzidis, M. G. *J. Am. Chem. Soc.* **2011**, *133*, 20476. (b) Bilc, D.; Mahanti, S. D.; Quarez, E.; Hsu, K. F.; Pcionek, R.; Kanatzidis, M. G. *Physical Review Letters* **2004**, *93*. (c) Sootsman, J. R.; Pcionek, R. J.; Kong, H. J.; Uher, C.; Kanatzidis, M. G. *Chemistry of Materials* **2006**, *18*, 4993−4995.

(14) Zhao, L.-D.; He, J.; Wu, C.-I.; Hogan, T. P.; Zhou, X.; Uher, C.; Dravid, V. P.; Kanatzidis, M. G. *J. Am. Chem. Soc.* **2012**, *134*, 7902.

(15) Hu, Z.; Gao, S. *Chem. Geol.* **2008**, *253*, 205.

(16) Androulakis, J.; Lee, Y.; Todorov, I.; Chung, D. Y.; Kanatzidis, M. G. *Phys. Rev. B* **2011**, *83*, No. 195209.

(17) Zhang, Q.; Wang, H.; Liu, W.; Wang, H.; Yu, B.; Zhang, Q.; Tian, Z.; Ni, G.; Lee, S.; Esfarjani, K.; Chen, G.; Ren, Z. *Energy Environ. Sci.* **2012**, *5*, 5246.

(18) (a) Wang, H.; Pei, Y.; LaLonde, A. D.; Snyder, G. J. *Adv. Mater.* **2011**, *23*, 1366. (b) Wang, H.; Pei, Y. Z.; LaLonde, A. D.; Snyder, G. J. *Proceedings of the National Academy of Sciences of the United States of America* **2012**, *109*, 9705−9709.

(19) Wang, S.; Zheng, G.; Luo, T.; She, X.; Li, H.; Tang, X. *J. Phys. D: Appl. Phys.* **2011**, *44*, No. 475304.

(20) Parker, D.; Singh, D. J. *Phys. Rev. B* **2010**, *82*, No. 035204.

(21) Biswas, K.; He, J.; Zhang, Q.; Wang, G.; Uher, C.; Dravid, V. P.; Kanatzidis, M. G. *Nat. Chem.* **2011**, *3*, 160.

(22) Biswas, K.; He, J.; Wang, G.; Lo, S.-H.; Uher, C.; Dravid, V. P.; Kanatzidis, M. G. *Energy Environ. Sci.* **2011**, *4*, 4775.

(23) Ohta, M.; Biswas, K.; Lo, S.-H.; He, J.; Chung, D. Y.; Dravid, V. P.; Kanatzidis, M. G. *Adv. Energy Mater.* **2012**, *2*, 1117.

(24) Biswas, K.; He, J.; Blum, I. D.; Wu, C.-I.; Hogan, T.; Seidman, D. N.; Dravid, V. P.; Kanatzidis, M. G. *Nature* **2012**, *489*, 414.

(25) Blachnik, R.; Igel, R. *Z. Naturforsch., B* **1974**, *29*, 625.

(26) Zhang, Q.; Cao, F.; Liu, W.; Lukas, K.; Yu, B.; Chen, S.; Opeil, C.; Broido, D.; Chen, G.; Ren, Z. *J. Am. Chem. Soc.* **2012**, *134*, 10031.

(27) Callaway, J. *Phys. Rev.* **1959**, *113*, 1046.

(28) Lo, S.-H.; He, J.; Biswas, K.; Kanatzidis, M. G.; Dravid, V. P. *Adv. Funct. Mater.* **2012**, *22*, 5175.

(29) Zhang, Y.; Ke, X.; Chen, C.; Yang, J.; Kent, P. R. C. *Phys. Rev. B* **2009**, *80*, 2009.

(30) He, J.; Androulakis, J.; Kanatzidis, M. G.; Dravid, V. P. *Nano Lett.* **2012**, *12*, 343.

(31) Hÿtch, M. J.; Snoeck, E.; Kilaas, R. *Ultramicroscopy* **1998**, *74*, 131.

(32) Dey, T. K.; Chaudhuri, K. D. *J. Low Temp. Phys.* **1976**, *23*, 419.

(33) He, J.; Girard, S. N.; Kanatzidis, M. G.; Dravid, V. P. *Adv. Funct. Mater.* **2010**, *20*, 764.